

Article

# Heat Transfer Enhancement and Entropy Generation of Nanofluids Laminar Convection in Microchannels with Flow Control Devices

Ping Li <sup>1</sup>, Yonghui Xie <sup>2</sup>, Di Zhang <sup>1,\*</sup> and Gongnan Xie <sup>3</sup>

<sup>1</sup> Key Laboratory of Thermal Fluid Science and Engineering of Ministry of Education, Xi'an Jiaotong University, Xi'an 710049, China; pingli@mail.xjtu.edu.cn

<sup>2</sup> School of Energy and Power Engineering, Xi'an Jiaotong University, Xi'an 710049, China; yhxie@mail.xjtu.edu.cn

<sup>3</sup> Department of Mechanical and Power Engineering, School of Marine Science and Technology, Northwestern Polytechnical University, Xi'an 710072, China; gongnan.xie@gmail.com

\* Correspondence: zhang\_di@mail.xjtu.edu.cn; Tel.: +86-29-8266-6559

Academic Editors: Giulio Lorenzini and Omid Mahian

Received: 15 February 2016; Accepted: 7 April 2016; Published: 21 April 2016

**Abstract:** The heat transfer enhancement and entropy generation of Al<sub>2</sub>O<sub>3</sub>-water nanofluids laminar convective flow in the microchannels with flow control devices (cylinder, rectangle, protrusion, and v-groove) were investigated in this research. The effects of the geometrical structure of the microchannel, nanofluids concentration  $\phi$  (0%–3%), and Reynolds number  $Re$  (50–300) were comparatively studied by means of performance parameters, as well as the limiting streamlines and temperature contours on the modified heated surfaces. The results reveal that the relative Fanning frictional factor  $fff_0$  of the microchannel with rectangle and protrusion devices are much larger and smaller than others, respectively. As the nanofluids concentration increases,  $fff_0$  increases accordingly. For the microchannel with rectangle ribs, there is a transition  $Re$  for obtaining the largest heat transfer. The relative Nusselt number  $Nu/Nu_0$  of the cases with larger nanofluids concentration are greater. The microchannels with cylinder and v-groove profiles have better heat transfer performance, especially at larger  $Re$  cases, while, the microchannel with the protrusion devices is better from an entropy generation minimization perspective. Furthermore, the variation of the relative entropy generation  $S'/S'_0$  are influenced by not only the change of  $Nu/Nu_0$  and  $fff_0$ , but also the physical parameters of working substances.

**Keywords:** nanofluids; microchannels; heat transfer enhancement; entropy generation; flow control devices

## 1. Introduction

Nanofluids, regarded as the new generation cooling working substances with high heat transfer enhancement performance, have been widely investigated from physical properties [1,2] to heat transfer characteristics [3,4] in recent years. Heris *et al.* [5] studied the CuO-water and Al<sub>2</sub>O<sub>3</sub>-water nanofluids flowing through an annular tube with a constant wall temperature in the laminar regime, and found that the heat transfer coefficient increased with the increase of nanofluids concentration and Peclet number, and the latter nanofluids obtained greater enhancement. Barzegarian *et al.* [6] investigated the heat transfer enhancement and pressure drop of TiO<sub>2</sub>-water nanofluids in the brazed plate heat exchanger, and found a significant increase in convective heat transfer coefficient, being enhanced by increasing nanofluids concentration, while, the increment in pressure drop was negligible. Andreozzi *et al.* [7] studied the turbulent forced convection of Al<sub>2</sub>O<sub>3</sub>-water nanofluids in symmetrically-heated ribbed channels, and the results showed that heat transfer increased with the

increase of nanofluids concentration and Reynolds number, but the pumping power also increased a lot. Moreover, the channel with triangle presented higher thermal performance and pressure losses. Sun *et al.* [8] found that the proposed nanofluids consisting of Cu nanoparticles, cetyltrimethyl ammonium chloride (CTAC), sodium salicylate (NaSal), and deionized water showed an improved drag-reducing performance and increased heat transfer coefficient. Hsieh *et al.* [9] conducted the experiments about spray cooling with nanofluids, and obtained a transient cooling curve and steady boiling curve, then found the average heat transfer coefficient and the associated critical heat flux significantly increased. Tsai *et al.* [10] investigated the flow and heat transfer of Au-water nanofluids in a heat pipe. The results showed that utilizing nanofluids as a working substance in heat pipes was promising to obtain large decreases of thermal resistance of heat pipes. Both the experimental and numerical studies about the flow resistance and heat transfer of nanofluids reveal that nanofluids give rise to considerable enhancement of heat transfer enhancement performance [11]. Additionally, the successful employment of nanofluids makes the heat transfer equipment more portable and smaller, so the process of miniaturization of heat transfer device is accelerated.

Microchannel heat sinks are an effective cooling technology to remove the large amount of heat from electronic systems. More recently, numerical and experimental researches about the flow and heat transfer characteristics of microchannels have been conducted [12–14]. Results suggested that the conventional Navier-Stokes analysis could be used in predicting heat transfer in a microchannel [15], and the correlation for the local Nusselt number was obtained. Furthermore, flow control technologies can be used to obtain desired flow structures in the internal flow, and they have been employed in the heat transfer enhancement researches. Liu *et al.* [16] investigated the turbulent flow and heat transfer characteristics in the proposed square channels with cylindrical grooves, and the results showed the heat transfer of proposed channels increased with reducing pressure drop. They [17] also studied the flow and heat transfer performances of rectangular dimpled channels with secondary protrusions, and found the secondary protrusion reduced the scale of recirculation flow in the next primary dimple, so the local heat transfer coefficient of the latter was improved. Additionally, both the heat transfer and pressure drop increased with the increase of the height of the secondary protrusions. Khan *et al.* [18] studied the thermal resistance and pressure drop of microchannels with various ribs in the laminar regime, and the results revealed that the lowest thermal resistance was observed in the microchannel with triangular ribs, and rectangular ribs produced the largest pressure drop. Recently, flow control technologies have also been introduced in the microchannels to achieve higher heat transfer enhancement, and the results showed strip-fins [19], wavy microchannel [20], and dimples/protrusions [21–23] were beneficial. Wei *et al.* [24] introduced dimples to the heat transfer enhancement of microchannel heat sinks, but the misuse of boundary conditions may lead to some discrepancies between the simulated results and real flow. The authors [25] investigated the laminar forced flow and heat transfer enhancement of a dimpled/protruded microchannel, and the detailed flow structures and performance parameters varying with physical properties and geometrical structures were analyzed, finally the correlations of friction factor and Nusselt number were obtained. Furthermore, we conducted the thermal performance of water in microchannels with grooves and obstacles in the laminar region. The results showed the combination structures of grooves and obstacles was beneficial for heat transfer enhancement [26]. The above studies show that application of flow control devices in microchannels could obtain a higher heat transfer coefficient in a forced convective flow.

In order to develop more high-efficiency, compact heat exchanger and microchannel heat sinks, the heat transfer enhancement and entropy generation of  $\text{Al}_2\text{O}_3$ -water nanofluids laminar convective flow in the microchannels with different flow control devices are investigated in this research. The effects of the geometrical structure of the microchannel, nanofluids concentration  $\varphi$  (0%–3%), and Reynolds number  $Re$  (50–300) are studied. The detailed flow structures, heat transfer performance and entropy generation are obtained and comparatively analyzed.

## 2. Physical Properties of Nanofluids

$\text{Al}_2\text{O}_3$  is a common and inexpensive nanoparticle, so it is selected as the nanoparticle of coolant in this research [27,28].  $\text{Al}_2\text{O}_3$ -water nanofluids are selected as working substances in this study [29,30], which are assumed as the mixtures of base fluid (water) and  $\text{Al}_2\text{O}_3$  nanoparticle with 30 nm diameter. The physical properties of the base fluid and  $\text{Al}_2\text{O}_3$  nanoparticle [31,32] are shown in Table 1, in which the reference temperature is 293 K. A single-phase model [33] is used to evaluate the physical properties of  $\text{Al}_2\text{O}_3$ -water nanofluids, and based on the assumptions that the aluminium oxide nanoparticle is spherical and homogeneously suspended in the base fluid, the following models are used to compute density, specific heat, dynamic viscosity, and thermal conductivity, respectively. Obtained from the above data and models, the physical properties of  $\text{Al}_2\text{O}_3$ -water nanofluids are shown in Table 2.

Density model:

$$\rho_{nf} = (1 - \phi) \rho_b + \phi \rho_p \quad (1)$$

Specific heat model:

$$C_{p_{nf}} = \frac{(1 - \phi) C_{p_b} \rho_b + \phi C_{p_p} \rho_p}{\rho_{nf}} \quad (2)$$

Dynamic viscosity model [34,35], which has been obtained by performing a precise least-square curve fitting of experimental data:

$$\mu_{nf} = \mu_b (123\phi^2 + 7.3\phi + 1) \quad (3)$$

Thermal conductivity (Bruggeman model) [36,37], which can be applied to spherical particle with various concentration of inclusion and obtained reasonable results:

$$k_{nf} = 0.25[(3\phi - 1)k_p + (2 - 3\phi)k_b + \sqrt{\Delta}] \quad (4)$$

$$\Delta = [(3\phi - 1)k_p + (2 - 3\phi)k_b]^2 + 8k_p k_b \quad (5)$$

**Table 1.** Physical properties of base fluid and  $\text{Al}_2\text{O}_3$  nanoparticle.

Substances	$D_p/\text{nm}$	$k/W \cdot \text{m}^{-1} \cdot \text{K}^{-1}$	$C_p/\text{J} \cdot \text{kg}^{-1} \cdot \text{K}^{-1}$	$\rho/\text{kg} \cdot \text{m}^{-3}$	$\mu/\text{Pa} \cdot \text{s}$
$\text{Al}_2\text{O}_3$	30	36.00	773.00	3880.00	-
Base fluid	-	0.60	4182.00	998.20	$9.93\text{e}-4$

**Table 2.** Physical properties of  $\text{Al}_2\text{O}_3$ -water nanofluids.

$\phi/\%$	$k/W \cdot \text{m}^{-1} \cdot \text{K}^{-1}$	$C_p/\text{J} \cdot \text{kg}^{-1} \cdot \text{K}^{-1}$	$\rho/\text{kg} \cdot \text{m}^{-3}$	$\mu/\text{Pa} \cdot \text{s}$
0.0	0.60	4182.00	998.20	$9.93\text{e}-4$
1.0	0.62	4053.21	1027.02	$1.08\text{e}-3$
2.0	0.63	3931.45	1055.84	$1.19\text{e}-3$
3.0	0.65	3816.16	1084.65	$1.32\text{e}-3$

## 3. Numerical Method and Validation

### 3.1. Governing Equations

Similar with our previous work [25], the incompressible steady Navier-Stokes equation is used to solve the flow and heat transfer in microchannels in this study, under the assumptions that the nanofluids flow is constant, the respective fluid properties, and negligible viscous dissipation. The governing equations are as follows:

Continuity equation:

$$\nabla \cdot \vec{u} = 0 \quad (6)$$

Momentum equation:

$$\rho_{nf} (\vec{u} \cdot \nabla) \vec{u} = -\nabla p + \mu_{nf} \nabla^2 \vec{u} \quad (7)$$

Energy equation:

$$\rho_{nf} C_{p_{nf}} (\vec{u} \cdot \nabla T) = k_{nf} \nabla^2 T \quad (8)$$

The SIMPLE method is used in coupling the pressure and velocity. The standard scheme is used for pressure discretization. The momentum and energy equations are solved with a second-order up-wind scheme. The residues of continuity, energy, and velocities are monitored to judge the convergence of computation, in which convergence criteria is set as  $1 \times 10^{-7}$ .

### 3.2. Geometrical Configuration of Models and Boundary Conditions

Fully developed periodic velocity and temperature can be obtained after some typical streamwise rows of flow control devices in the microchannels. The main domain of the microchannels is a periodic unit in the flow and heat transfer. Under this condition, it is desirable to choose the smallest repetitive unit as the computational domain to minimize the computational expense. Cross-sections of microchannels with cylinder, rectangle, and v-groove devices and the flow domain of the microchannel with protrusions in a periodic unit are shown in Figure 1. The microchannel is  $150 \mu\text{m}$  ( $W$ )  $\times$   $50 \mu\text{m}$  ( $H$ ) in cross-section, and the flow control devices are arranged on the surface with a width of  $200 \mu\text{m}$  and the relative depth  $\delta/D = 0.2$ . The coordinates  $x$ ,  $y$ ,  $z$  in Figure 1 represent the streamwise, spanwise, and normalwise directions, respectively, in the simulation model. A uniform constant heat flux of  $q'' = 5 \times 10^5 \text{ W}\cdot\text{m}^{-2}$  and no-slip boundary condition are specified at the four external surfaces of the microchannel in the  $y$  and  $z$  directions. Transitional periodic boundary condition is applied at the inlet and outlet. Nanofluids flows into the transitional domain in the positive  $x$  direction from inlet surface with a fully developed velocity and bulk temperature of 300 K, in which the inlet  $Re$  ranges from 50 to 300, and nanofluids concentration are set as 0%–3%, named as water, nano1, nano2, nano3, respectively.

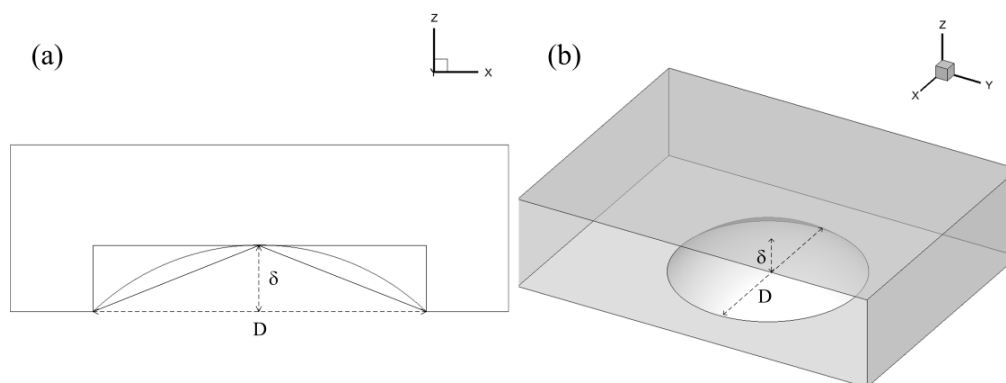


**Figure 1.** Models of microchannels with flow control devices: (a) cross-sections of microchannels with cylinder, rectangle, and v-groove devices; and (b) flow domain of the microchannel with protrusions.

### 3.3. Data Reduction

In this research, the Reynolds number is defined by:

$$\text{Re} = \frac{\rho_{nf} U_{ave} D_h}{\mu_{nf}} \quad (9)$$

where  $U_{ave}$  is the average velocity of inlet,  $D_h$  is hydraulic diameter and defined by:

$$D_h = \frac{2WH}{W + H} \quad (10)$$

The Nusselt number is given by:

$$Nu = \frac{hD_h}{k_{nf}} \quad (11)$$

where  $k_{nf}$  is the thermal conductivity of nanofluids,  $h$  is the heat transfer coefficient and described as:

$$h = \frac{q''}{\Delta T} \quad (12)$$

where  $q''$  represents the heat flux, and  $\Delta T$  is the difference of mean wall temperature  $T_{w,ave}$  and mean fluids temperature  $T_{nf,ave}$ :

$$\Delta T = T_{w,ave} - T_{nf,ave} \quad (13)$$

The Fanning friction factor  $f$  is defined as:

$$f = -\frac{(\Delta p/L)D_h}{2\rho_{nf}U_{ave}^2} \quad (14)$$

where  $\Delta P$  is the pressure drop and  $L$  is the streamwise microchannel length.

The entropy generation in the forced conductive flow with heat transfer contains two parts, one due to the heat transfer irreversibility, and the other accounting for the fluid frictional irreversibility [38]. The entropy generation of flow for nanofluids can be calculated by the following equations [39,40]:

$$S' = \frac{k}{T^2} (|\nabla T|)^2 + \frac{\mu}{T} \left( \frac{\partial U_i}{\partial x_j} + \frac{\partial U_j}{\partial x_i} \right) \frac{\partial U_i}{\partial x_j} = S'_T + S'_F \quad (15)$$

$$S'_T = \frac{k}{T^2} (|\nabla T|)^2 \quad (16)$$

$$S'_F = \frac{\mu}{T} \left( \frac{\partial U_i}{\partial x_j} + \frac{\partial U_j}{\partial x_i} \right) \frac{\partial U_i}{\partial x_j} \quad (17)$$

For an internal flow in the proposed microchannels, the rate of entropy generation per unit length can be calculated as [41]:

$$S' = \frac{1}{\pi Nu} \frac{q'^2}{kT^2} + \frac{m^3 f}{\pi^2 \rho^2 T r^5} \quad (18)$$

And,  $q'$  and  $r$  can be given as:

$$q' = 2\pi r_0 q'', r = \frac{D_h}{2} \quad (19)$$

Therefore, Equation (18) can be given as:

$$S' = \frac{q''^2 \pi D^2}{kT^2 Nu} + \frac{32m^3 f}{\pi^2 \rho^2 T D^5} = S'_T + S'_F \quad (20)$$

Furthermore, the baseline Fanning friction factor  $f_0$  and Nusselt number  $Nu_0$  for a smooth rectangular microchannel of the analytical solutions of Shah and London [42], as well as the resulting entropy generation  $S'_0$ , are used to normalize the Fanning friction factor, Nusselt number, and entropy generation in this research.

### 3.4. Model Validation

For the purpose of increasing the accuracy and validity of the model, an all-hexahedral mesh is generated and refined. To balance the simulation accuracy and computational resource, a grid independence validation is carried out to determine reasonable grid nodes for computational analysis at the case of  $q'' = 5 \times 10^5 \text{ W} \cdot \text{m}^{-2}$ ,  $T_{in} = 300 \text{ K}$ ,  $Re = 200$  with water as working substance (Table 3), taking a microchannel with protrusions as an example. In the validation procedure, the Nusselt number and Fanning friction factor are selected as the evaluation criteria, starting from a coarse mesh and refining it until the characteristic parameters are independent of the mesh size. As is shown, the relative discrepancies of  $f$  and  $Nu$  are 0.10% and 0.89% when the mesh changes from mesh3 to mesh4, respectively. Therefore, the proposed mesh is mesh3. Grid independence is similarly established for the other microchannels.

**Table 3.** Grid independence validation.

	Nodes	$Nu$	Difference %	$f \times 10$	Difference %
1	498,920	5.775	12.68	1.370	5.71
2	1,163,056	5.125	5.87	1.296	3.52
3	2,452,800	4.841	0.10	1.252	0.89
4	5,689,802	4.836	-	1.241	-

The above solution method is validated by simulating the flow and heat transfer of a base fluid (water) in a smooth microchannel, in which the computational domain has a height of  $200 \mu\text{m}$ , a width of  $50 \mu\text{m}$ , and a length of  $150 \mu\text{m}$ . The results from the proposed model is compared with referenced results from Shah and London's [42] research, and the largest difference is 0.92% (Table 4), which means that the proposed model could be employed to simulate the flow and heat transfer in microchannels in the cases of working substances with constant physical properties.

**Table 4.** Simulation model validation.

Re	fRe			Nu		
	Referenced Result	Proposed Model	Difference%	Referenced Result	Proposed Model	Difference%
50	18.233	18.136	-0.53	2.94	2.930	-0.35
100	18.233	18.300	-0.37	2.94	2.914	0.87
200	18.233	18.344	0.61	2.94	2.954	0.46
300	18.233	18.401	-0.92	2.94	2.957	-0.59

## 4. Results and Discussions

### 4.1. Effects of Structures

The variations trend of  $fff_0$ ,  $Nu/Nu_0$  and  $S'/S'_0$  are similar for different nanofluid concentration cases, so the results of  $\varphi = 2\%$  are shown as examples herein to illustrate the effects of structures.

The relative Fanning friction factor  $fff_0$  (Figure 2) of microchannel with rectangle and protrusion devices are much larger and smaller than others, respectively, and increase a little as  $Re$  increases. While,  $fff_0$  of microchannels with cylinder and v-groove devices are medium, and increase quickly with the increase of  $Re$ . To investigate the variation of  $fff_0$  influenced by the microchannel structures in detail, the flow structures analysis can be employed. In the studied microchannels,  $fff_0$  consists of frictional resistance and form drag. The development of flow boundary layer is interrupted due to the presence of flow control devices, and then the frictional resistance decreases. However, the flow separation occurs near the flow control devices, so the form drag increases. Figure 3 shows the limiting streamlines and temperature contours of the four microchannels in the case of  $\varphi = 2\%$  and

$Re = 100$ . For the microchannel with cylinder (Figure 3a) devices, flow separates at the tail end of the cylinder, and reattaches in the central upstream of next period domain. The start of flow separation is wide in the channel in the spanwise direction, so the forepart of the separation bubble nearly fills the whole channel. After leaving the cylinder zone, the separation flow reattaches directing the central flow quickly, and finally reattaches near the inlet of the next period domain, forming a large separation bubble, so the whole separation bubble shows a trapezoid-like structure. Then the form drag increases a lot and, therefore, the increase of form drag and  $f/f_0$  of the microchannel with cylinder is maximum. For the microchannel with rectangle (Figure 3b) devices, part of the main flow impinges directly on the front surface of rectangle and flows backward to the previous period domain from the inlet. While, near the back surface, the cross-section is suddenly enlarged, and then the adverse pressure gradient forms herein, so the backflow from the front of the next period domain flows directly to the back surface of the rectangle, and turns to the main flow, finally, flowing to the outlet together with the main flow. Therefore, the flow domains both ahead and behind the rectangle devices are filled with the separation flow, then the form drag increases sharply. For the microchannel with protrusions (Figure 3c), the main flow impinges on the front of the protrusion, just leaving curving streamlines on the surface. While the flow separates at the tail end of the protrusion due to the formation of a local adverse pressure gradient, and the separation flow reattaches quickly in the wake, so the small separation bubble herein makes the form drag increase slightly. Therefore, the increase of the form drag and  $f/f_0$  of the microchannel with protrusions is a minimum. For the microchannel with v-groove (Figure 3d) devices, the main flow flows through the front part of the channel with curving streamlines, then separates in the central back of the v-groove devices and reattaches in the wake, so the separation bubble shows a spindle-like structure. Moreover, two small corner vortices form near the walls, due to the combined effects of the non-slip wall and advanced pressure gradient in the channel in the spanwise direction. Furthermore, comparing with that of the microchannel with cylinder devices, the separation bubble locates in the back of channel, not affecting the next period domain. Therefore, the increase of form drag and  $f/f_0$  herein is less than that of the microchannel with cylinder devices. What is more, as the mass flow rate and  $Re$  increase, the separation flow in the microchannels with flow control devices are enhanced, more or less, so their  $f/f_0$  increase gradually.

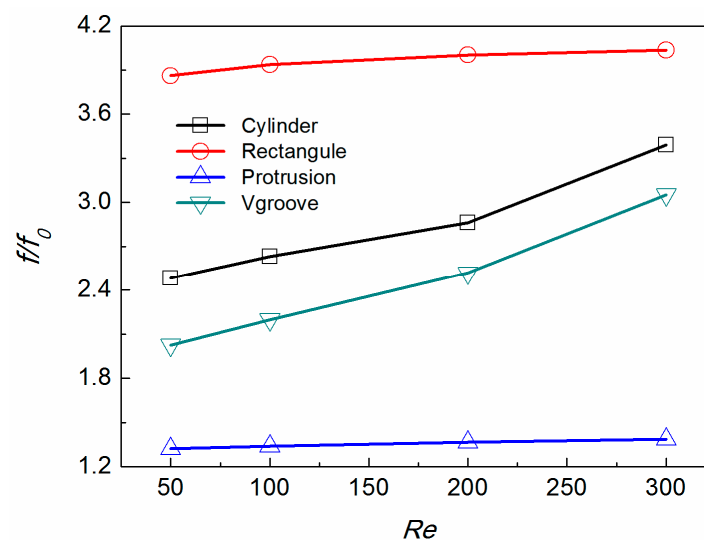
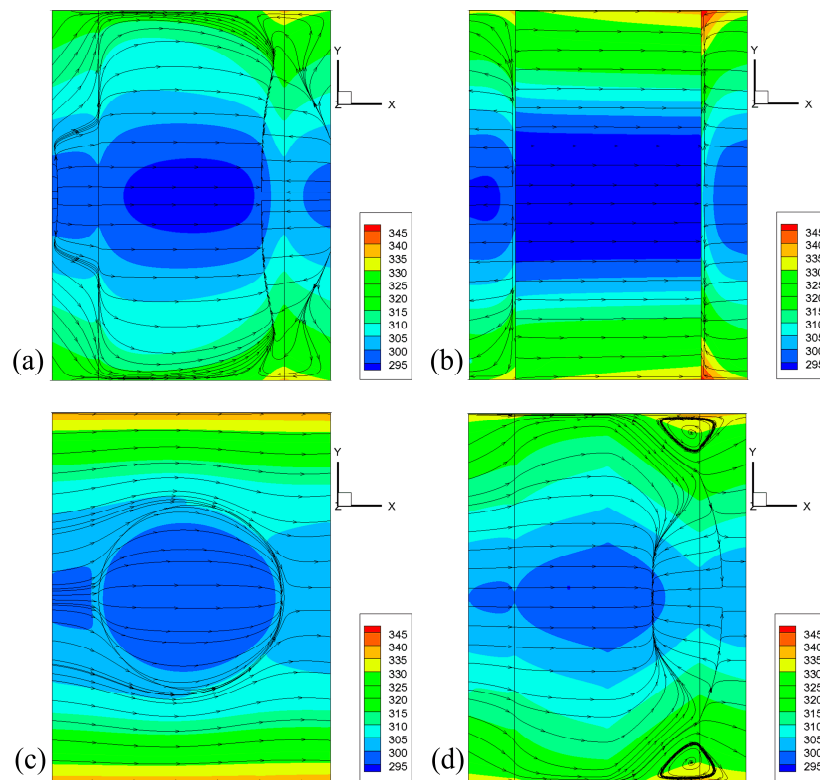


Figure 2. Variation of  $f/f_0$  in different microchannels (nano2).



**Figure 3.** Temperature contours (unit: K) and limiting streamlines on the modified heated surface (nano2,  $Re = 100$ ): (a) cylinder; (b) rectangle; (c) protrusion; and (d) v-groove devices.

The variation trend of relative Nusselt number  $Nu/Nu_0$  are more complex than that of  $ff_0$ . As Figure 4 shows,  $Nu/Nu_0$  of microchannel with cylinder devices are larger than that of others, and, at low  $Re$  cases ( $Re = 50$  and  $100$ ),  $Nu/Nu_0$  of microchannel with protrusion devices are minimum, while, as  $Re$  further increases to  $200$  and  $300$ ,  $Nu/Nu_0$  of microchannel with rectangle are smaller than that of others.  $Nu/Nu_0$  of all microchannels increase with the increase of  $Re$ , except that of microchannel with rectangle devices. Analyzing from temperature contour on the heated surfaces (Figure 3), heat transfer in the zones before separation, reattachment, and wake, heat transfer is better. It indicates that high heat transfer region is caused by the reattachment and the vortices shedding from the flow control devices, and the low heat transfer region locates in the region of flow separation. In the microchannel with cylinder (Figure 3a) devices, the large separation bubble fills the back of the channel and the front of the next period domain, especially enhancing the heat and mass transfer between the central flow and the near wall flow in the spanwise direction, and then the average temperature and temperature gradient are the lowest, so its  $Nu/Nu_0$  is larger than others. In the microchannel with rectangle (Figure 3b) devices, separation flow almost fills both ahead and behind the rectangle, but the heat and mass transfer between the central flow and the near wall flow in the spanwise direction is weakened, then the temperature gradient and average temperature increases, so  $Nu/Nu_0$  is lower. In the microchannel with protrusion (Figure 3c) devices, the higher temperature and larger temperature gradient are observed, so  $Nu/Nu_0$  is minimum herein. In the microchannel with v-groove (Figure 3d) devices, although the large separation bubble forms in the back of the channel, showing the enhancement of heat and mass transfer between the central flow and the near wall flow in the spanwise direction, the central low temperature region is small, so the average temperature is medium. Furthermore, as the mass flow rate and  $Re$  increase, the separation flow in the microchannels with cylinder, protrusion, and v-groove devices are enhanced, more or less, so their  $Nu/Nu_0$  increase gradually. Especially, for the microchannel with rectangle devices, starting from the minimum  $Re$  case ( $Re = 50$ ), the large-scale separation flow forms and locates ahead and behind of the rectangle, when  $Re$

increases, the separation flow fills the whole of these regions, so the main flow no longer impinges directly on the front surface of the rectangle, and the direct contact area between the main flow and the heated surfaces decreases; therefore, the heat transfer is reduced. Meanwhile, when  $Re$  increases, the heat transfer coefficient of heated surfaces increases, and the local heat transfer is enhanced. Therefore, for the microchannel with rectangle devices, there must be a transition point of  $Re$  for obtaining the largest heat transfer. In the above studied cases, the transition point is  $Re = 100$ . Finally, it can be concluded that not only the scale and intensity of the separation flow, but also the development of the separation bubble in the spanwise direction, can give rise to the  $Nu/Nu_0$ .

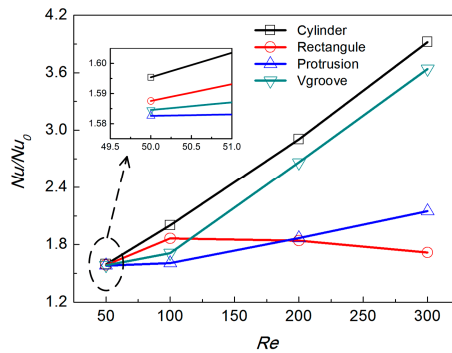


Figure 4. Variation of  $Nu/Nu_0$  in different microchannels (nano2).

Based on the entropy generation theory and Equation (20), for the given working condition, the entropy generation of microchannel increases with the increase of pressure drop (reflected by Fanning friction factor) and the decrease of heat transfer (reflected by the Nusselt number). Furthermore, due to the nonlinear effect of mass flow rate, the influences of Fanning friction factor on the entropy generation for varied  $Re$  cases are obviously different from that of the Nusselt number. Similar with the above analysis, the relative entropy generation  $S'/S'_0$  of  $\varphi = 2\%$  due to the heat transfer irreversibility and the fluid frictional irreversibility is calculated and shown in Figure 5. The results reveal that the microchannel with protrusion devices shows favorable entropy generation performance. For the microchannel with rectangle, the large  $ff_0$  and relative small  $Nu/Nu_0$  make its relative large  $S'/S'_0$ , especially at larger  $Re$  cases, so this structure is not suitable for the studied working conditions. The  $Nu/Nu_0$  of microchannels with cylinder and v-groove devices are large enough, but the  $ff_0$  are also large, so the  $S'/S'_0$  are larger than that of microchannels with protrusion devices in most cases. The results shows that  $S'/S'_0$  are more influenced by  $ff_0$  at the larger  $Re$  cases, while, more influenced by  $Nu/Nu_0$  at the smaller  $Re$  cases. What is more, the microchannels with cylinder and v-groove devices have better heat flux transfer performance, while the microchannel with protrusion devices is better from the perspective of entropy generation minimization.

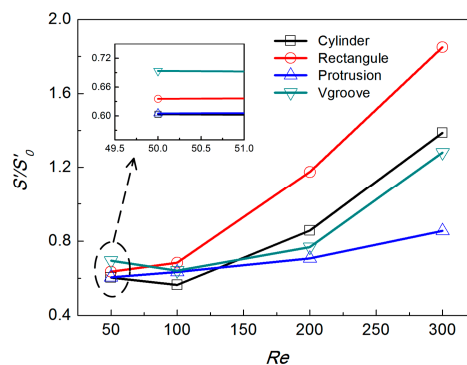


Figure 5. Variation of  $S'/S'_0$  in different microchannels (nano2).

#### 4.2. Effects of Nanofluids Concentration

As are shown in the above results, the microchannel with protrusion devices shows favorable performance in entropy generation minimization, especially at larger Reynolds number cases, and then the variations trend of  $fff_0$ ,  $Nu/Nu_0$  and  $S'/S'_0$  of the protruded microchannel are shown as examples herein to illustrate the effects of nanofluids concentration.

Figure 6 is the variation of  $fff_0$  in the protruded microchannel with working substances varying from water to nano3.  $fff_0$  increases with the increase of  $Re$ . For the same  $Re$ ,  $fff_0$  show a small difference among different fluids, while, as the nanofluids concentration increases,  $fff_0$  increases a bit accordingly. When  $Re$  increases, the above-mentioned differences get obvious. Figure 7 shows the temperature contours and limiting streamlines on the protruded surface. Flow separates at the tail end of the protrusion, and reattaches quickly in the wake under the effect of the adverse pressure gradient, so the separation bubbles are small. As the nanofluid concentration increases, separation bubbles show little change in the streamwise direction, while the effect of protrusion on flow structure and temperature develops along the spanwise direction, then  $fff_0$  increases slightly.

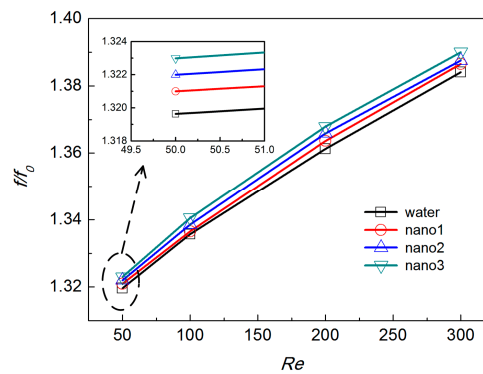


Figure 6. Variation of  $fff_0$  in a microchannel with protrusion devices.

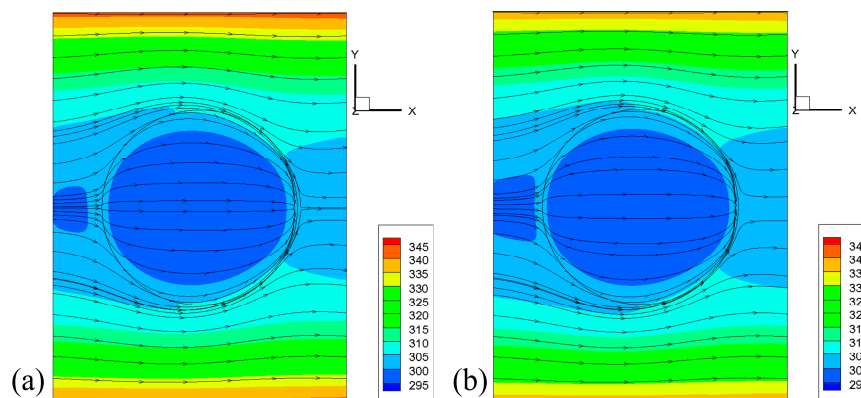


Figure 7. Temperature contours (unit: K) and limiting streamlines on the protruded surface ( $Re = 100$ ): (a) nano1; and (b) nano2.

The variation trend of  $Nu/Nu_0$  is more obvious, comparing with that of  $fff_0$ . As are shown in Figure 8,  $Nu/Nu_0$  of the cases with larger nanofluids concentrations are larger. When  $Re$  is relatively small ( $Re = 50$  and  $100$ ), only a small difference can be observed among different working substances. As  $Re$  further increases to  $200$  and  $300$ ,  $Nu/Nu_0$  of all the cases increase sharply, which is due to the quick development of separation bubbles, and then the differences of  $Nu/Nu_0$  among different working substances also becomes obvious. As are shown in Figure 7, as nanofluid concentration increases, the effect of separation flow develops along the spanwise direction, enhancing the heat and mass transfer

between near wall fluid and the main flow; therefore, the average temperature and temperature gradient decreases, and the temperature of the surfaces in the spanwise direction decreases, obviously, so  $Nu/Nu_0$  of the whole channel increases. Furthermore, this influence is enhanced at larger  $Re$  cases.

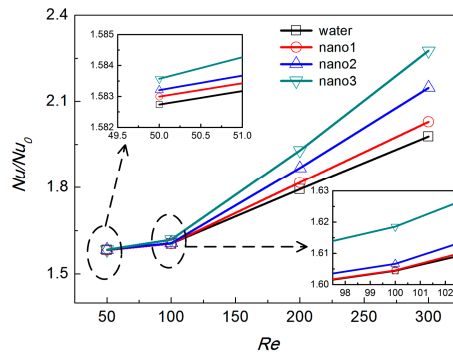


Figure 8. Variation of  $Nu/Nu_0$  in microchannel with protrusion.

The variation of  $S'/S'_0$  in the protruded microchannel with working substances varying from water to nano3 are shown in Figure 9. When  $Re$  is 50,  $S'/S'_0$  of the water case is at a maximum, and as nanofluid concentration increases,  $S'/S'_0$  decreases gradually, combining with the results in Figures 7 and 8 the variation of  $S'/S'_0$  herein means the influence of  $Nu/Nu_0$  is dominant for small  $Re$  cases. As  $Re$  increases,  $S'/S'_0$  of cases with larger nanofluids concentration increase more quickly, and then  $S'/S'_0$  of nano3 case is maximum at  $Re = 200$  and  $300$ , which means that the mass flow rate and  $ff_0$  have combined dominant effects for large  $Re$  cases. As  $Re$  increases, differences of  $S'/S'_0$  among different cases with varied working substances also increase.

Furthermore,  $S'/S'_0$  consists of the heat transfer irreversibility and the fluid frictional irreversibility, which can be evaluated by  $S_T'/S'_0$  and  $S_F'/S'_0$ , respectively, and due to the large increase in the form drag, the fluid friction induced entropy generation can no longer be negligible [41], different with that in low flow resistance applications [43]. The variation of  $S_T'/S'_0$  and  $S_F'/S'_0$  are shown in Figure 10 to illustrate the change of  $S'/S'_0$  in detail. For the given  $Re$ , as nanofluids concentration increases,  $S_T'/S'_0$  decreases and  $S_F'/S'_0$  increases. With the increases of nanofluids concentration, both the thermal conductivity of  $Al_2O_3$ -water nanofluids (Table 2) and  $Nu/Nu_0$  (Figure 8) increase. Then, based on the Equation (20),  $S_T'/S'_0$  decreases. While, with the increases of nanofluids concentration, the density of working substances increases (Table 2), but  $ff_0$  (Figure 7) and mass flow rate also increase, and the change of the latter two parameters are much larger than that of former, then  $S_F'/S'_0$  increases. As  $Re$  increases, both  $Nu/Nu_0$  and  $ff_0$  increase, so  $S_T'/S'_0$  decreases, but  $S_F'/S'_0$  increases accordingly. The variation of  $S'/S'_0$  is based on the change of  $S_T'/S'_0$  and  $S_F'/S'_0$ , which are all influenced by not only the change of  $Nu/Nu_0$  and  $ff_0$ , but also the physical parameters of the working substances.

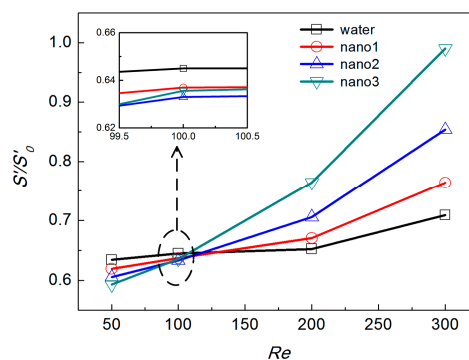


Figure 9. Variation of  $S'/S'_0$  in the microchannel with protrusion devices.

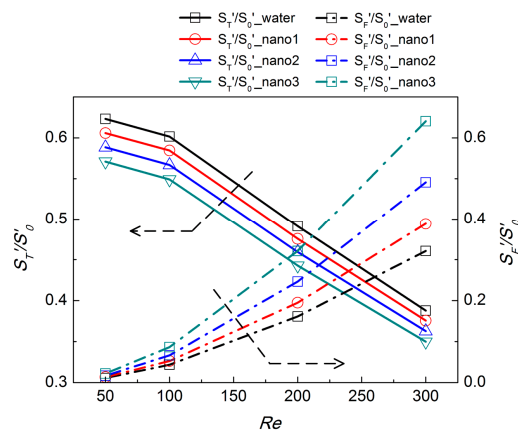


Figure 10. Variation of  $S_T'/S'_0$  and  $S_F'/S'_0$  in the microchannel with protrusion devices.

## 5. Conclusions

The heat transfer enhancement and entropy generation of  $\text{Al}_2\text{O}_3$ -water nanofluids laminar convective flow in the microchannels with flow control devices (cylinder, rectangle, protrusion and v-groove ribs) are investigated in this research, in which the nanofluids concentration vary from 0% to 3%, and the Reynolds number range from 50 to 300. The detailed conclusions are as follows.

- (1)  $fff_0$  of the microchannel with rectangle and protrusion ribs are much larger and smaller than others, respectively, and increase a little as  $Re$  increases. While,  $fff_0$  of the microchannels with cylinder and v-groove ribs are medium, and increase quickly with the increase of  $Re$ . As the nanofluids concentration increases,  $fff_0$  increases a bit, accordingly, and this trend is enhanced when  $Re$  increases.
- (2)  $Nu/Nu_0$  of the microchannel with cylinder ribs are larger than others, and, at low  $Re$  cases ( $Re = 50$  and  $100$ ),  $Nu/Nu_0$  of the microchannel with protrusion ribs are a minimum, while, as  $Re$  further increases to 200 and 300,  $Nu/Nu_0$  of the microchannel with rectangle ribs are smaller than that of others.  $Nu/Nu_0$  of all the microchannels increase with the increase of  $Re$ , except that of the microchannel with rectangle ribs. For the microchannel with rectangle ribs, there is a transition point of  $Re$  for obtaining the largest heat transfer.  $Nu/Nu_0$  of the cases with larger nanofluids concentration are higher. The differences of  $Nu/Nu_0$  among different working substances increase with the increase of  $Re$ .
- (3) The microchannels with cylinder and v-groove ribs have the better heat flux transfer performance, especially at larger  $Re$  cases, while the microchannel with protrusion ribs is better from the perspective of entropy generation minimization. The variation of  $S'/S'_0$  is based on the change of  $S_T'/S'_0$  and  $S_F'/S'_0$ , which are all influenced by not only the change of  $Nu/Nu_0$  and  $fff_0$ , but also the physical parameters of the working substances.

**Acknowledgments:** The authors acknowledge the financial support from the National Natural Science Foundation of China (Grant No. 51506162).

**Author Contributions:** All authors have worked on this manuscript together, including the proposal of initial research concept and the design of research, as well as the data analysis and writing of manuscript, and all authors have read and approved the final manuscript.

**Conflicts of Interest:** The authors declare no conflict of interest.

## Nomenclature

$C_p$	Fluid special heat ( $\text{J} \cdot \text{kg}^{-1} \cdot \text{K}^{-1}$ )
$D$	Dimple/Protrusion print diameter ( $\mu\text{m}$ )
$D_h$	Characteristic length
$f$	Fanning friction factor
$H$	Microchannel height ( $\mu\text{m}$ )
$h$	Heat transfer coefficient ( $\text{W} \cdot \text{m}^{-2} \cdot \text{K}^{-1}$ )
$k$	Fluid thermal conductivity ( $\text{W} \cdot \text{m}^{-1} \cdot \text{K}^{-1}$ )
$m$	Flow rate ( $\text{kg} \cdot \text{s}^{-1}$ )
$Nu$	Nusselt number
$P$	Fluid pressure (Pa)
$q'$	Heat transfer rate per unit length ( $\text{W} \cdot \text{m}^{-1}$ )
$q''$	Surface heat flux rate ( $\text{W} \cdot \text{m}^{-2}$ )
$Re$	Reynolds number
$S'$	Entropy generation ( $\text{W} \cdot \text{K}^{-1} \cdot \text{m}^{-1}$ )
$S_F'$	Friction induced entropy generation ( $\text{W} \cdot \text{K}^{-1} \cdot \text{m}^{-1}$ )
$S_T'$	Heat transfer induced entropy generation ( $\text{W} \cdot \text{K}^{-1} \cdot \text{m}^{-1}$ )
$T$	Temperature (K)
$U_{ave}$	Average velocity of inlet ( $\text{m} \cdot \text{s}^{-1}$ )
$\Delta P$	Pressure drop (Pa)
$\Delta T$	Mean temperature difference (K)

## Greek symbols

$\delta$	Dimple/protrusion depth ( $\mu\text{m}$ )
$\phi$	Nanoparticle volume fraction (%)
$\rho$	Fluid density ( $\text{kg} \cdot \text{m}^{-3}$ )

## Subscripts

$h$	Hydraulic
$w$	Wall
$o$	Baselines condition

## References

1. Wang, X.Q.; Mujumdar, A.S. Heat transfer characteristics of nanofluids: A review. *Int. J. Therm. Sci.* **2007**, *46*, 1–19. [[CrossRef](#)]
2. Xu, J.; Bandyopadhyay, K.; Jung, D. Experimental investigation on the correlation between nano-fluid characteristics and thermal properties of  $\text{Al}_2\text{O}_3$  nano-particles dispersed in ethylene glycol-water mixture. *Int. J. Heat Mass Transf.* **2016**, *94*, 262–268. [[CrossRef](#)]
3. Hussien, A.A.; Abdullah, M.Z.; Moh'd, A.A.N. Single-phase heat transfer enhancement in micro/minichannels using nanofluids: Theory and applications. *Appl. Energy* **2016**, *164*, 733–755. [[CrossRef](#)]
4. Lo, K.J.; Weng, H.C. Convective heat transfer of magnetic nanofluids in a microtube. *Smart Sci.* **2015**, *3*, 56–64.
5. Heris, S.Z.; Etemad, S.G.; Esfahany, M.N. Experimental investigation of oxide nanofluids laminar flow convective heat transfer. *Int. Commun. Heat Mass* **2006**, *33*, 529–535. [[CrossRef](#)]
6. Barzegarian, R.; Moraveji, M.K.; Aloueyan, A. Experimental investigation on heat transfer characteristics and pressure drop of BPHE (brazen plate heat exchanger) using  $\text{TiO}_2$ -water nanofluid. *Exp. Therm. Fluid Sci.* **2016**, *74*, 11–18. [[CrossRef](#)]

7. Andreozzi, A.; Manca, O.; Nardini, S.; Ricci, D. Forced convection enhancement in channels with transversal ribs and nanofluids. *Appl. Therm. Eng.* **2016**, *98*, 1044–1053. [[CrossRef](#)]
8. Sun, B.; Zhang, Z.; Yang, D. Improved heat transfer and flow resistance achieved with drag reducing Cu nanofluids in the horizontal tube and built-in twisted belt tubes. *Int. J. Heat Mass Transf.* **2016**, *95*, 69–82. [[CrossRef](#)]
9. Hsieh, S.S.; Liu, H.H.; Yeh, Y.F. Nanofluids spray heat transfer enhancement. *Int. J. Heat Mass Transf.* **2016**, *94*, 104–118. [[CrossRef](#)]
10. Tsai, C.Y.; Chien, H.T.; Ding, P.P.; Chan, B.; Luh, T.Y.; Chen, P.H. Effect of structural character of gold nanoparticles in nanofluid on heat pipe thermal performance. *Mater. Lett.* **2004**, *58*, 1461–1465. [[CrossRef](#)]
11. Sarafraz, M.M.; Hormozi, F. Heat transfer, pressure drop and fouling studies of multi-walled carbon nanotube nano-fluids inside a plate heat exchanger. *Exp. Therm. Fluid Sci.* **2016**, *72*, 1–11. [[CrossRef](#)]
12. Lee, P.S.; Garimella, S.V.; Liu, D. Investigation of heat transfer in rectangular microchannels. *Int. J. Heat Mass Transf.* **2005**, *48*, 1688–1704. [[CrossRef](#)]
13. Hung, T.C.; Yan, W.M. Optimization of a microchannel heat sink with varying channel heights and widths. *Numer. Heat Transf. A* **2012**, *62*, 722–741. [[CrossRef](#)]
14. Mohammed, H.A.; Gunnasegaran, P.; Shuaib, N.H. Influence of channel shape on the thermal and hydraulic performance of microchannel heat sink. *Int. Commun. Heat Mass Transf.* **2011**, *38*, 474–480. [[CrossRef](#)]
15. Gunnasegaran, P.; Mohammed, H.A.; Shuaib, N.H.; Saidur, R. The effect of geometrical parameters on heat transfer characteristics of microchannels heat sink with different shapes. *Int. Commun. Heat Mass Transf.* **2010**, *37*, 1078–1086. [[CrossRef](#)]
16. Liu, J.; Xie, G.N.; Simon, T.W. Turbulent flow and heat transfer enhancement in rectangular channels with novel cylindrical grooves. *Int. J. Heat Mass Transf.* **2015**, *81*, 563–577. [[CrossRef](#)]
17. Liu, J.; Song, Y.; Xie, G.N.; Sunden, B. Numerical modeling flow and heat transfer in dimpled cooling channels with secondary hemispherical protrusions. *Energy* **2015**, *79*, 1–19. [[CrossRef](#)]
18. Khan, A.A.; Kim, S.M.; Kim, K.Y. Performance Analysis of a microchannel heat sink with various rib configurations. *J. Thermophys. Heat Transf.* **2015**, *29*, 1–9. [[CrossRef](#)]
19. Hong, F.; Cheng, P. Three dimensional numerical analyses and optimization of offset strip-fin microchannel heat sinks. *Int. Commun. Heat Mass Transf.* **2009**, *36*, 651–656. [[CrossRef](#)]
20. Sui, Y.; Teo, C.J.; Lee, P.S.; Chew, Y.T.; Shu, C. Fluid flow and heat transfer in wavy microchannels. *Int. J. Heat Mass Transf.* **2010**, *53*, 2760–2772. [[CrossRef](#)]
21. Lan, J.B.; Xie, Y.H.; Zhang, D. Flow and heat transfer in microchannels with dimples and protrusions. *J. Heat Transf.* **2012**, *134*, 021901. [[CrossRef](#)]
22. Bi, C.; Tang, G.H.; Tao, W.Q. Heat transfer enhancement in mini-channel heat sinks with dimples and cylindrical grooves. *Appl. Therm. Eng.* **2013**, *55*, 121–132. [[CrossRef](#)]
23. Silva, C.; Park, D. Optimization of fin performance in a laminar channel flow through dimpled surfaces. *J. Heat Transf.* **2009**, *131*, 021702. [[CrossRef](#)]
24. Wei, X.J.; Joshi, Y.K.; Ligrani, P.M. Numerical simulation of laminar flow and heat transfer inside a microchannel with one dimpled surface. *J. Electron. Packag.* **2007**, *129*, 63–70. [[CrossRef](#)]
25. Li, P.; Zhang, D.; Xie, Y.H. Heat transfer and flow analysis of Al<sub>2</sub>O<sub>3</sub>-water nanofluids in microchannel with dimple and protrusion. *Int. J. Heat Mass Transf.* **2014**, *73*, 456–467. [[CrossRef](#)]
26. Xie, Y.H.; Shen, Z.Y.; Zhang, D.; Lan, J.B. Thermal performance of a water-cooled microchannel heat sink with grooves and obstacles. *J. Electron. Packag.* **2014**, *136*, 021001. [[CrossRef](#)]
27. Hung, T.C.; Yan, W.M.; Wang, X.D.; Chang, C.Y. Heat transfer enhancement in microchannel heat sinks using nanofluids. *Int. J. Heat Mass Trans.* **2012**, *55*, 2559–2570.
28. Ho, C.; Chen, W.C.; Yan, W.M. Correlations of heat transfer effectiveness in a minichannel heat sink with water-based suspensions of Al<sub>2</sub>O<sub>3</sub> nanoparticles and/or MEPCM particles. *Int. J. Heat Mass Transf.* **2014**, *69*, 293–299. [[CrossRef](#)]
29. Kuppusamy, N.R.; Mohammed, H.; Lim, C. Numerical investigation of trapezoidal grooved microchannel heat sink using nanofluids. *Thermochim. Acta* **2013**, *573*, 39–56. [[CrossRef](#)]
30. Tokit, E.M.; Mohammed, H.A.; Yusoff, M. Thermal performance of optimized interrupted microchannel heat sink (IMCHS) using nanofluids. *Int. Commun. Heat Mass Transf.* **2012**, *39*, 1595–1604. [[CrossRef](#)]
31. Chun, B.H.; Kang, H.U.; Kim, S.H. Effect of alumina nanoparticles in the fluid on heat transfer in double-pipe heat exchanger system. *Korean J. Chem. Eng.* **2008**, *25*, 966–971. [[CrossRef](#)]

32. Manca, O.; Nardini, S.; Ricci, D.; Tamburrino, S. Numerical investigation on mixed convection in triangular cross-section ducts with nanofluids. *Adv. Mech. Eng.* **2012**, *4*, 139370. [[CrossRef](#)]
33. Manca, O.; Mesolella, P.; Nardini, S.; Ricci, D. Numerical study of a confined slot impinging jet with nanofluids. *Nanoscale Res. Lett.* **2011**, *6*, 1–16. [[CrossRef](#)] [[PubMed](#)]
34. Maiga, S.E.B.; Palm, S.J.; Nguyen, C.T.; Roy, G.; Galanis, N. Heat transfer enhancement by using nanofluids in forced convection flows. *Int. J. Heat Fluid Flow* **2005**, *26*, 530–546. [[CrossRef](#)]
35. Duangthongsuk, W.; Wongwises, S. An experimental study on the heat transfer performance and pressure drop of TiO<sub>2</sub>-water nanofluids flowing under a turbulent flow regime. *Int. J. Heat Mass Transf.* **2010**, *53*, 334–344. [[CrossRef](#)]
36. Vajjha, R.S.; Das, D.K. Experimental determination of thermal conductivity of three nanofluids and development of new correlations. *Int. J. Heat Mass Transf.* **2009**, *52*, 4675–4682. [[CrossRef](#)]
37. Mahian, O.; Kianifar, A.; Kleinstreuer, C.; Moh'd, A.A.N.; Pop, I.; Sahin, A.Z.; Wongwises, S. A review of entropy generation in nanofluid flow. *Int. J. Heat Mass Transf.* **2013**, *65*, 514–532. [[CrossRef](#)]
38. Ko, T.H.; Ting, K. Entropy generation and optimal analysis for laminar forced convection in curved rectangular ducts: A numerical study. *Int. J. Therm. Sci.* **2006**, *45*, 138–150. [[CrossRef](#)]
39. Bejan, A. General criterion for rating heat-exchanger performance. *Int. J. Heat Mass Transf.* **1978**, *21*, 655–658. [[CrossRef](#)]
40. Bejan, A. A study of entropy generation in fundamental convective heat transfer. *J. Heat Trans.* **1979**, *101*, 718–725. [[CrossRef](#)]
41. Singh, P.K.; Anoop, K.B.; Sundararajan, T.; Das, S.K. Entropy generation due to flow and heat transfer in nanofluids. *Int. J. Heat Mass Transf.* **2010**, *53*, 4757–4767. [[CrossRef](#)]
42. Shah, R.K.; London, A.L. *Laminar Flow Forced Convection in Ducts*; Academic Press: New York, NY, USA, 1978.
43. Huminic, G.; Huminic, A. Heat transfer and entropy generation analyses of nanofluids in helically coiled tube-in-tube heat exchangers. *Int. Commun. Heat Mass Transf.* **2016**, *71*, 118–125. [[CrossRef](#)]



© 2016 by the authors; licensee MDPI, Basel, Switzerland. This article is an open access article distributed under the terms and conditions of the Creative Commons Attribution (CC-BY) license (<http://creativecommons.org/licenses/by/4.0/>).